



# Simulation-based approach to estimate influencing factors on acoustic resonance spectra of additively manufactured mechanical metamaterials

Silviya M. Boyadzhieva<sup>a</sup>, Florian Gutmann<sup>b</sup>, Sarah C.L. Fischer<sup>a,\*</sup>

<sup>a</sup> Fraunhofer Institute for Nondestructive Testing IZFP, Campus E3.1, 66123 Saarbrücken, Germany

<sup>b</sup> Fraunhofer Institute for High-Speed Dynamics, Ernst Mach Institute EMI, Ernst Zermelo Street 4, 79104 Freiburg, Germany

## ARTICLE INFO

### Keywords:

Mechanical metamaterials  
Resonance testing  
Vibration modes  
Acoustics  
Additive manufacturing  
Non-destructive testing

## ABSTRACT

Acoustic Resonance Testing is a nondestructive testing method based on the analysis of eigenfrequencies of structures. While it is a well-established technique for conventionally manufactured parts, more research is needed to use the technique to quantify the properties of complex, filigree structures like additively manufactured parts. Therefore, this work examines simulation-based generation of synthetic data to estimate influencing factors caused by additive manufacturing. Using numerical eigenfrequency analysis, a systematic study of the vibration modes of a Ti6Al4V metamaterial unit cell with multistable mechanical behaviour reveals the interplay between the material properties, geometrical parameters and manufacturing-induced defects. The simulations enable the identification of specific eigenfrequencies for which the highest influence of manufacturing variations on the vibration modes are to be expected in experiments, for example, with regards to the Young's modulus, spring width, or deflection-induced change in geometry. Frequency shift plots visualize the predicted effects of different parameters and form the basis for future guided experimental design and analysis for complex structures. The simulation-based approach allows a screening of multiple influencing factors, which is not possible experimentally. The simulation-based generation of synthetic data will contribute to the improvement of the interpretation of acoustic spectra and will extend the acoustic resonance testing for more complex structures.

## 1. Introduction

Acoustic Resonance Testing (ART) is a low-cost nondestructive evaluation option suitable for a high number of similar components. This technique relies on the ability of solids to vibrate with characteristic frequencies, i.e. their eigenfrequencies, combined in an acoustic fingerprint. A variation in the shape, dimensions, material or mechanical properties, such as the elastic modulus or density, lead to a change in frequency or amplitude. Through external energy input, for example, a hammer impact, structure vibrations can be excited and detected by microphones, high speed cameras or laser vibrometer and represented as resonant peaks in the frequency spectrum. A comparison of the position and shape of peaks in the spectra of different parts allows a fast and reliable distinction between a defective part and a reference part assumed as "ideal", or distinction between parts of the same family with parameter variations, such as variations of a metamaterial unit cell [1–4].

ART has a wide application field and has been used for the inspection of cast brake calipers [5], automotive steering knuckles [6], cast iron microstructures [7], recognition of coins [8], ceramic capacitors [9] or glass bottles [10] as well for the determination

\* Corresponding author.

E-mail address: [sarah.fischer@izfp.fraunhofer.de](mailto:sarah.fischer@izfp.fraunhofer.de) (S.C.L. Fischer).

of fruit firmness, for example of apples [11] or melons [12]. Recently, the acoustic testing has been used for characterization of additively manufactured lattice structures, for example, for determination of the elastic modulus [13,14] or the detection of missing rods [15]. While there are studies on nondestructive characterization using computed tomography [16–18] or, as mentioned above, acoustic techniques, the complexity of additively manufactured structures and, especially, metamaterials still poses challenges for their characterization compared to parts with bulk properties [19]. To adapt the technique to the upcoming trends in material development, improvements and specifically simulation-aided approaches will be required in order to apply ART to more complex geometries and manufacturing processes.

A trend in the development of new parts is the integration of functions through tailored material properties or geometry. In this context, mechanical metamaterials summarize the class of materials where a designed architecture allows the achievement of unusual physical mechanical properties [20,20–22]. Throughout the present article, the term metamaterials exclusively refers to the class of mechanical metamaterials. Popular representatives are lattice, pentamode, auxetic, chiral as well as origami and kirigami-inspired structures [23–28]. The fabrication of such complex designs is often demanding and realized by additive manufacturing [29–32]. Laser powder bed fusion (LPBF) is one of the most commonly used for the fabrication of metallic structures. The building process consist of alternating powder application and its local melting by a laser beam. Steel [33,34], titanium [35] and nickel [29] based alloys are established materials for this process while copper [36,37] represents a challenge. Ti6Al4V, for example, is frequently studied for manufacturing of metamaterials, in particular for lattice like structures due to its good suitability for three-dimensional (3D) printing among with compatibility to living tissue, corrosion resistance, high strength and elastic modulus by relatively low density [38,39]. Despite the high flexibility in geometry and material, the industrial use of the process faces certain challenges. Besides the long fabrication duration and limitations in terms of part dimensions as well as the number of parts per print, process induced defects and irregularities can occur. Moreover, the as-built and as-designed structure can differ from each other in various aspects. Notably, waviness, shrinkage, lack of fusion or powder adhesion are commonly observed. These can result in a high surface roughness, residual stresses, high porosity and an appearance of cracks [40–42].

Even though ART is an established method for rapid volumetric inspection, there are limitations when it comes to specimens with small volume, complex structure and presence of many superposing influencing factors such as in additively manufactured parts. In this case, the interpretation of the frequency spectra can be impaired by the overlapping of different defects. ART is often accompanied by finite element method simulations for verification and an in-depth investigation of the structural vibration performance [6,43–46]. There are few studies focusing on the generation of synthetic data for conventionally manufactured parts to inform experimental techniques and improve the method to provide quantitative rather than just qualitative information [6,45]. Simulation-based quantification of the influence of manufacturing induced defects or variations on acoustic spectra has not been widely investigated, especially for additively manufactured samples.

Therefore, this work focuses on the generation of synthetic data of eigenfrequencies to understand the multitude of variable properties of complex additively manufactured parts. The main goal is to systematically quantify the influence of manufacturing-induced geometry and material property variations as this is not experimentally feasible. A metamaterial unit cell, developed by Kappe et al. [47] in a previous publication, was studied. Due to its relatively small dimensions, complex design and presence of process induced deformation, the model structure poses a challenge for the ART and is selected as a suitable representative of the class of mechanical metamaterials for testing of the presented approach. The model cell consists of two main structure elements, a spring and two snap-fit arms, enabling a higher mechanical damping than feasible by the bulk material (Ti6Al4V) itself. Thereby, the choice of the spring and arm width is crucial since it determines the achievable mechanical behaviour, namely a bistable or self-recovering state.

Based on the 3D model of the unit cells, finite element analysis of the eigenfrequencies is performed taking into account the effect of geometric irregularities and a variation in Young's modulus. Subsequently, effects of the width of the spring and snap-fit arm are studied numerically. The investigation focuses on quantifying the expected impact that the corresponding parameters have on the vibration modes of the unit cell. In the future, the generated synthetic data can support interpretation of ART spectra and enable a prediction of possible frequency shifts as a result of certain defects. This study contributes to the improvement of ART for additively manufactured parts and can hopefully contribute to the establishment of reliable, cost-effective quality control methods for metamaterial parts in industry.

In the following section, the model unit cell is described in detail followed by an introduction of the simulation methods and model modifications. Afterwards, a systematic numerical study of eigenfrequencies of the model unit cells is presented and results analysed according to the influencing factors: cell geometry, distortion, displacement and elastic modulus. The results are summarized in terms of multimodal frequency shift maps to study the effects of combinations of influencing factors. Lastly, the findings are discussed, highlighting some of the challenges and potential for future work in the area of ART for metamaterials.

## 2. Materials and methods

### 2.1. Metamaterial model structure: Geometrical structure and manufacturing process of friction based unit cell

In the following section, a concise description of the tested geometry is provided. This study focused on the vibration behaviour of a new metamaterial unit cell, shown in Fig. 1,a, with outer dimensions of about 1 cm × 1 cm × 3 cm. The design and manufacturing of the cell was systematically studied by the authors in a previous publication [47]. The cell consists of a spring, two snap-fit mechanisms and a supporting structure on each side. The geometry design allows a reduction of the Young's modulus (from 110 GPa for Ti6Al4V as bulk material to 1.2–2.7 GPa) and an increase of the loss coefficient up to 0.2 comparable to polymeric foams and

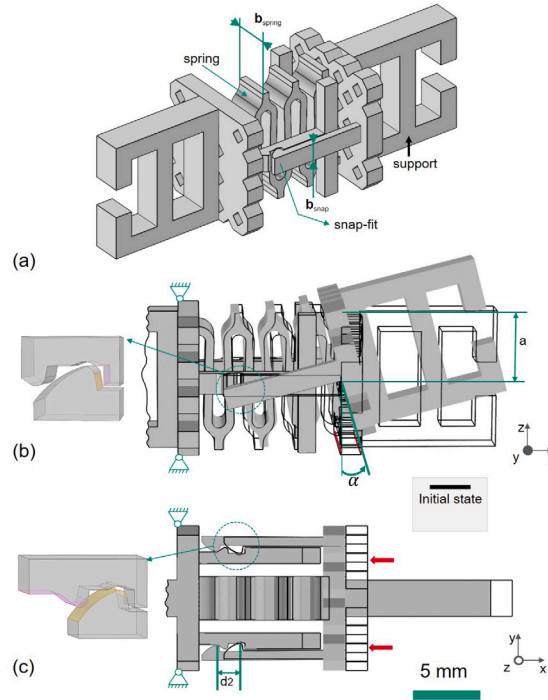


**Fig. 1.** Unit cell geometry. (a) A representative 3D model of the investigated metamaterial unit cell composed of a spring, parallel orientated snap-fit mechanisms, and a supporting structure on both ends. Depicted is a unit cell of type V1.2 with  $b_{\text{spring}} = 3$  mm and  $b_{\text{snap}} = 1.5$  mm. (b) Fabrication induced distortion of the structure. The red highlighted margins correspond to the edges on which a prescribed displacement of  $a \cdot \tan(\alpha)$  with  $a = 5$  mm is applied to induce deformation. (c) Model change after compression i.e. a prescribed displacement  $d_2 = 1.3$  mm (the red arrows indicate the direction). On the left, the surface elements of the snap-fit mechanism allocated to the contact pair in the simulation as a source (purple) and a destination (yellow) element is shown. The outline in black represents the nominal geometry. (For interpretation of the references to colour in this figure legend, the reader is referred to the web version of this article.)

engineering polymers. The used material (Ti6Al4V), on the other hand, allows an application at temperatures of more than 1000 °C, significantly higher than the operating temperature of common polymeric materials. During deformation, the spring element stores elastic energy and the arm elements allow energy absorption and dissipation through friction.

The mechanical performance of the cell is mainly dictated by the width combination of the two elements, since the width affects their stiffness. The ratio of  $b_{\text{snap}}/b_{\text{spring}}$  serves as a reference criterion. With a ratio of 0.5 or smaller, a self recovering behaviour and a ratio higher than 0.5 a bi-stable state can be realized. For instance, a cell with  $b_{\text{snap}} = 1.5$  mm,  $b_{\text{spring}} = 3$  mm and ratio of 0.5 (designated as V1.2) can be assessed as self-recovering while V3.1 with  $b_{\text{snap}} = 4.5$  mm,  $b_{\text{spring}} = 1.5$  mm and ratio of 3 as bi-stable. In other words, after a sufficiently high compressive force is applied, enabling one arm of the snap-fit mechanism to overcome the elevation (Fig. 1,c), V1.2 returns to the initial state with no external force required, while V3.1 remains in a second stable state. The energy stored in the deformation of the spring in case of V1.2 is sufficiently high that bending of the arm and elevation re-overcoming occurs. In case of V3.1 an external force is required for a state change.


Five different combinations of  $b_{\text{snap}}$  and  $b_{\text{spring}}$ , respectively five cell types, were produced. These are designated as V1.2, V1.3, V2.2, V3.1 and V3.2 (Table 1). Samples of these types were provided for this study to enable experimental measurements using ART. For completeness and to ensure a broader parameter variation, four additional types (V1.1, V2.1, V2.3 and V3.3 (Table 1)) were considered in the simulation. The structures were manufactured from Ti6Al4V powder (layer thickness 20  $\mu\text{m}$ ) in a Laser Powder Bed Fusion system (LPBF, EOS M 100) using a 200 W laser (CW-laser, YLR-series, wavelength 1070 nm) [47].

From the listed cell variations (Table 1), five specimens of types V1.2, V1.3, V2.2, V3.1 and V3.2 were considered for further investigations. The structures were manufactured in the same conditions as detailed above. More detailed information about the fabrication process and structure design has already been published in a previous work by Kappe et al. [47].

## 2.2. Simulations

An eigenfrequency analysis was carried out in the environment of Comsol Multiphysics to investigate specific effects of a certain geometry deviation on the vibration behaviour of the presented structure. The *Solid Mechanics* physic interface and an *Eigenfrequency* study in the *Structural Mechanics* module were used to determine the natural frequency values and visualize the corresponding natural modes. Thereby a free vibration is considered. The geometry was meshed with tetrahedron elements with maximum size of 0.4 mm, minimum size of 0.1 mm, and an average element quality of 0.66.

**Table 1**  
Unit cell designation according to the combination of spring and snap-fit nominal width.



Designation	V1.1	V1.2	V1.3	V2.1	V2.2	V2.3	V3.1	V3.2	V3.3
$b_{\text{spring}}/\text{mm}$	1.5	3	4.5	1.5	3	4.5	1.5	3	4.5
$b_{\text{snap}}/\text{mm}$	1.5	1.5	1.5	3	3	3	4.5	4.5	4.5

To realize a distortion and compression induced deformation in the unit cell a prescribed displacement node was added to the *Solid Mechanics* physic interface and a non-linearity including *Stationary* study was performed. A tetrahedron mesh with maximum element size of 2.65 mm, minimum size of 0.02 mm, and an average element quality of 0.64 was built in the case of a distorted structure (see geometry in Fig. 1,b). In the case of a deformation (Fig. 1,c), the values were adapted to 0.8 mm, 0.05 mm and 0.66, respectively.

The material constants for the elastic modulus  $E = 110$  GPa and the density  $\rho = 4410$  kg/m<sup>3</sup> were assigned to the structure, regardless of geometry type, based on material data sheets of the used Ti6Al4V powder. The Poisson's ratio  $\nu = 0.28$  was adapted from the literature [48].

### 2.3. Implementation of geometric changes in the CAD model

With regard to the geometrical structure (Fig. 1), a variation in the spring and snap-fit arm width, as well as deformation induced deviation from the initial state were considered. An out of plane deformation (Fig. 1,b, further designated as deflection) and a deformation of the structure caused by compression (Fig. 1,c, further designated as displacement) were recreated by a stationary study enclosing non-linearity in Comsol Multiphysics.

In Section 3.1, the results concerning deflection of the structure will be presented. To determine the boundaries for the simulations, the deflection of the samples was analysed with an optical microscope (KEYENCE VHX-600, Profile measurement unit VHX-S15, Japan), on at least 3 different positions. Among these, a distortion angle of 1 to 12° was observed, which was most pronounced for unit cell V1.2 and V1.3 and on average  $10 \pm 2^\circ$ . Therefore, the following section of the study is focused on these cell types. An illustration of the process of obtaining a deformed geometry is shown in Fig. 1,b and c. Deflection was simulated by utilizing boundary conditions in Comsol Multiphysics: one side of the structure was defined as fixed constraint and on the opposite side, specifically on the red marked lines, a defined edge displacement of  $d_1 = a \cdot \tan(\alpha) \cdot p$  with ( $a = 5$  mm) (Fig. 1,b) was applied. A parameter sweep over  $\alpha$ , from 1 to 15° with 1° degree increments was performed. To prevent overlapping in the area of the snap-fit arms, contact pairs containing the two opposite surfaces were defined: yellow (Fig. 1,b, destination) and purple (Fig. 1,b, source). The deformed geometry at each angle step was then exported as a .stl file and used for the natural frequency studies.

In Section 3.2, the results for the cell deformation, caused by a compression in the  $x$ -direction, are presented (Fig. 1,c). The boundary conditions for this simulation were determined based on the geometrical limitations of the unit cells. In case of compression beyond a displacement of 1.6 mm in  $x$ -direction, the arm elements collide with the supporting ends. In the simulation a similar approach, as described above, was followed to create a pressed geometry (Fig. 1,c). On the non-fixed side, a predefined displacement  $d_2 \cdot p$  was included, where  $d_2$  varied from 0 to 1.3 mm in 0.1 mm steps. The faces specified as a contact pair are shown in Fig. 1,c,left.

In both cases, a penalty factor of 1 and a friction coefficient of 0.5 were set. The contact pair function requires a sufficiently fine meshing. To avoid convergence problems, the displacement ( $d_1$  and  $d_2$ ) was additionally multiplied by the parameter  $p$  and a sweep over  $p$  from 0 to 1 was performed. The increment size was set at 0.01, in the case of  $d_1$  and 0.05 for  $d_2$ .

## 3. Results

A systematic numerical study of different influencing factors on the model structure was performed to collect synthetic data for acoustic eigenfrequencies. The systematic study considers design-related features (variation of feature sizes such as spring and snap-fit width), manufacturing-related flaws (a distortion and a variation in the Young's modulus) as well as function-related effects (a deformation in the spring and snap-fit arm induced by compression).

For each geometry, the first fifty to sixty natural modes i.e. eigenvalues were calculated. The data obtained was used to determine whether, and to what extent, the deformation of the structure affects the vibration behaviour.

### 3.1. The impact of geometry

In the following, we investigated whether a differentiation between the cell types is possible with regard to the width of the main structure elements (spring and snap-fit arms). As mentioned before, the element's width determines the mechanical behaviour of the cell. The proposed approach is based on the comparison of particular modes of which the vibration was primarily manifested by deformation of one of the main elements (spring or snap-fit arms). Two modes (1 and 2) dominated by the spring deformation and two other modes dominated by the snap-fit arm deformation (3 and 4) were empirically selected (Fig. 2). Modes 1 and 2 exhibited an increase in the eigenfrequency for higher spring width and were nearly independent of the change in arm width. For example, an increase in spring width from 1.5 mm to 4.5 mm resulted in a frequency shift of about 250 Hz (mode 1) and 200 Hz (mode 2). A

change in the snap-fit width from 1.5 mm to 4.5 mm induced a decrease in frequency up to  $-33$  Hz (mode 1) and  $-43$  Hz (mode 2). In comparison, the eigenvalues of modes 3 and 4 change with variation in the spring width by a maximum of 16 Hz. In particular, mode 3 appeared to reach a high frequency shift of  $\approx 1780$  Hz compared to  $\approx 140$  Hz for mode 4 when the arm width increased to 4.5 mm (Fig. 2). Thus, a classification could be performed based on preselected vibration modes reacting with a high change in eigenvalue due to the variation in geometry parameters. Supported by the study in the previous sections, and by taking into account the accuracy of the ART equipment, a suitable frequency range can be established, in which potential irregularities (e.g. deflection) would have the lowest impact.

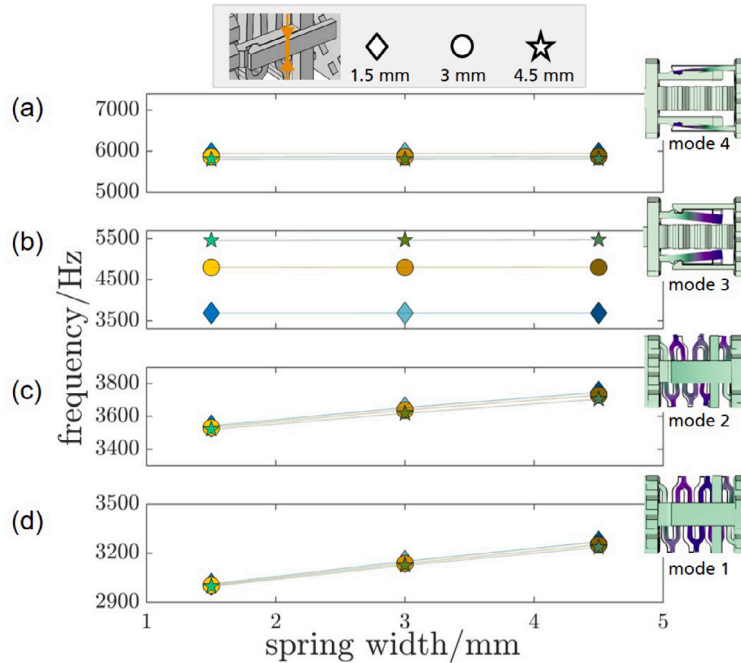


Fig. 2. Eigenfrequency values of four selected vibration modes in dependence of the spring and snap-fit arm width. The symbols rhombus, circle and star designate the thickness of the arm element. Mode 1 (d) and mode 2 (c) are mostly dominated by the deformation of the spring. Mode 3 (b) and mode 4 (a) are dominated by deformation of the snap-fit arms. The study was conducted for  $E = 110$  GPa.

### 3.2. The impact of distortion

The effect of distortion on the structure's vibration modes was investigated up to 40 kHz in order to remain in accordance with the specifications of typical microphones used for experimental ART studies. To keep the graph concise, only the modes for which the predicted frequency change is higher than 50 Hz are included in Fig. 3. The omitted data points were nevertheless plotted in Fig. A.9. 50 Hz was chosen as a cut-off independently of the frequency although sensitivity of actual microphones might vary to simplify the interpretation.

In the audible range of the frequency spectrum, the majority of the eigenvalues of the deflected structure show a frequency shift ( $\delta f$ ) under 50 Hz in relation to the ideal condition ( $f_0$ ). Up to 20 kHz, the expected maximum  $\delta f$  by a maximum deflection angle of  $15^\circ$  was 69 Hz (for V1.2, at  $f_0 = 16590$  Hz) and 91 Hz (for V1.3, at  $f_0 = 16590$  Hz). The frequency shift appeared to be more pronounced in the range above 20 kHz. For instance, a symmetrical change in  $\delta f$  at  $f_0 = 29677$  Hz and  $f_0 = 29737$  Hz for V1.2, and at  $f_0 = 29848$  Hz and  $f_0 = 29926$  Hz for V1.3 can be observed, which corresponds to peak splitting in a frequency spectrum. This implies that for an “ideal” sample, the distance between the two peaks should be 100 Hz and, depending on the resolution of the measurement system, it may occur as a single broad peak. Distortion leads to an increase in the distance within those eigenvalue (i.e. peak) pairs of 152 Hz at the angle of  $5^\circ$  and 565 Hz at  $15^\circ$  for V1.2, and 138 Hz ( $5^\circ$ ) and 549 Hz ( $15^\circ$ ) for V1.3 (Fig. 3).

Based on the results of the simulations, a distinct trend in the frequency change over the distortion between  $0^\circ$  to  $15^\circ$  can be identified and easily fitted by fundamental functions. This allows a fast prediction of how much a certain resonant peak is expected to change by a given distortion angle. Using a second-order polynomial, the data for selected modes most affected by the kind of deformation were fitted and illustrated in Fig. 4. The calculated coefficients are listed in Table 2. The difference in spring width between V1.2 and V1.3 did not affect the progression of the  $\delta f(x)$  curve over the angular range, when identical modes were considered (Fig. 4). Furthermore, not all modes were equally affected by the variation in distortion angle. For example, the vibration mode with an initial frequency value of 36767 Hz for V1.2 and 32008 Hz for V1.3 (marked in green, Fig. 4) reached a slope of about  $30$  Hz/ $^\circ$  and  $24$  Hz/ $^\circ$ , respectively. In comparison, the slope of  $\delta f(x)$  for the modes with  $f_0 = 21132$  Hz (1.2) and  $f_0 = 21751$  Hz (1.3) increased and was about  $11$  Hz/ $^\circ$  and  $10$  Hz/ $^\circ$ . Only these modes with a sufficiently high  $\delta f(x)'$  are suitable for deduction of the degree of distortion based on the frequency shift.

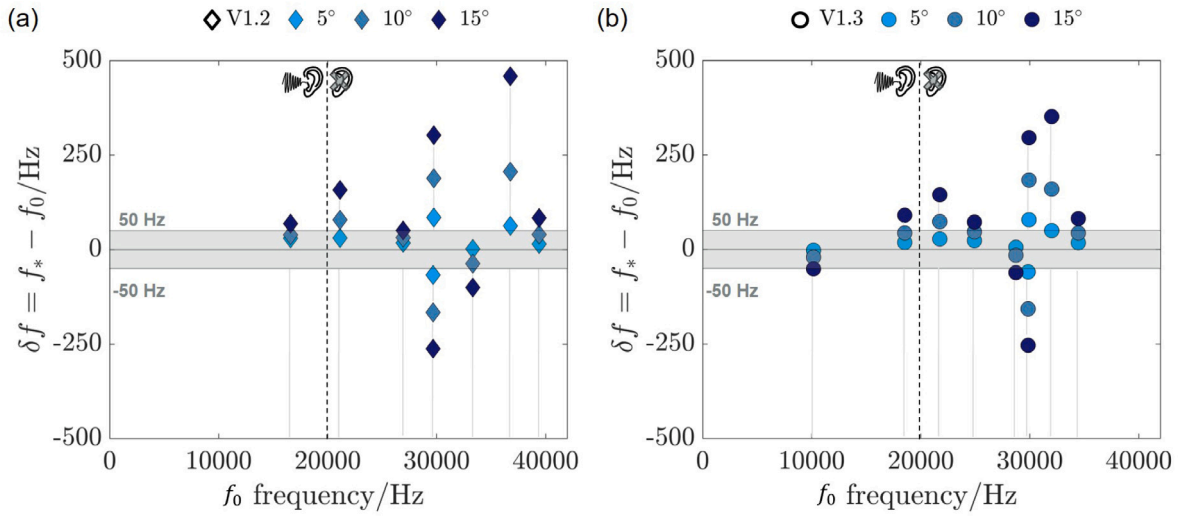


Fig. 3. Predicted shift in natural frequency due to structure deflection of 5°, 10° and 15° in the case of two unit cells: (a) V1.2 ( $b_{\text{spring}} = 3 \text{ mm}$  and  $b_{\text{snap}} = 1.5 \text{ mm}$ , left) and (b) V1.3 ( $b_{\text{spring}} = 4.5 \text{ mm}$  and  $b_{\text{snap}} = 1.5 \text{ mm}$ , right). Only natural frequencies reaching a shift of more than 50 Hz are shown for better readability. The complete data set is shown in Fig. A.9 for 15°.

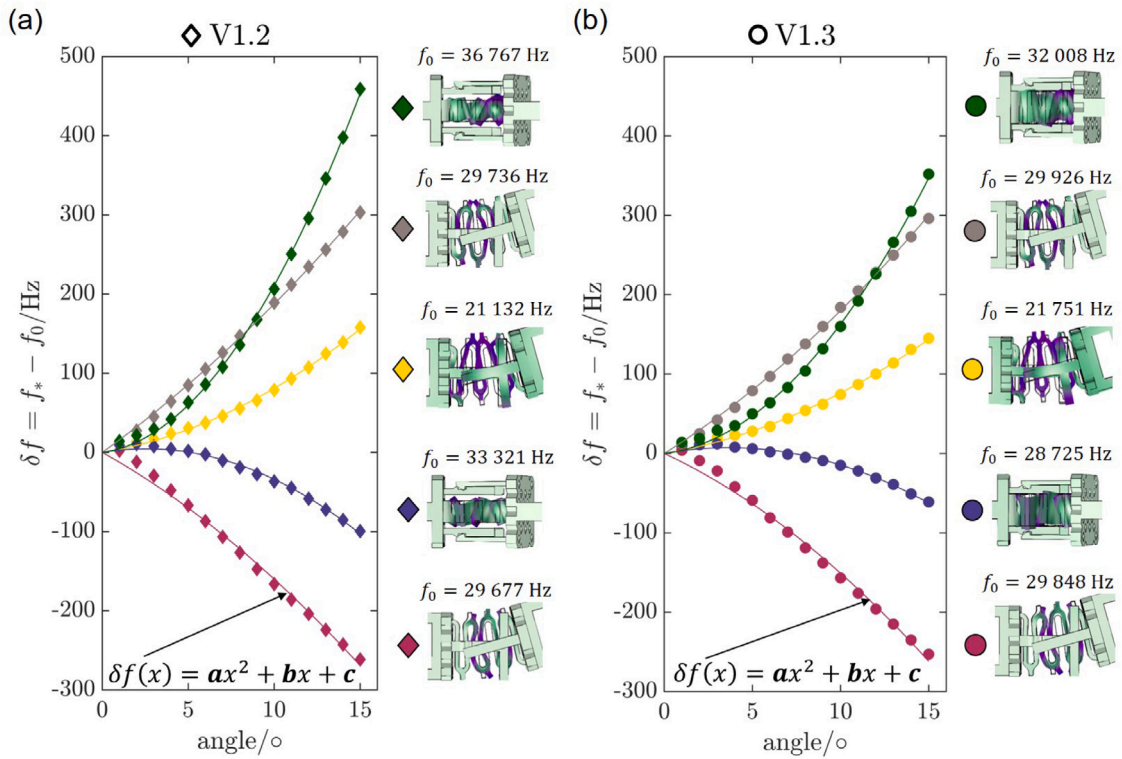


Fig. 4. Expected shift in natural frequency over the considered deflection range of 1° to 15° for certain vibration modes for two different unit cells: (a) V1.2 and (b) V1.3. Modes were empirically selected based on predicted vibration nature so that they are likely affected by the geometry change due to distortion. The regression functions were generated in Matlab and the coefficients determined can be found in Table 2. (For interpretation of the references to colour in this figure legend, the reader is referred to the web version of this article.)

**Table 2**

Coefficients  $a$ ,  $b$  and  $c$  related to the fit function  $\delta f = ax^2 + bx + c$  plotted in Fig. 4 and calculated by Matlab. The intersection point on the y-axis was set to zero.

V1.2				V1.3			
$f_0/\text{Hz}$	$a$	$b$	$c$	$f_0/\text{Hz}$	$a$	$b$	$c$
36 767	1.8	2.8	$-5.9 * 10^{-23}$	32 008	1.4	2.7	$-1.6 * 10^{-22}$
29 763	0.3	15.5	$3.2 * 10^{-10}$	29 926	0.4	14	$3.3 * 10^{-10}$
21 132	0.5	3.5	$-2.4 * 10^{-10}$	21 751	0.4	3.7	$-4.6 * 10^{-11}$
33 321	-0.7	3.5	$-5 * 10^{-11}$	28 725	-0.5	4	$1.9 * 10^{-10}$
29 677	-0.4	-12	$-1.6 * 10^{-22}$	29 848	-0.5	-10	$1.1 * 10^{-19}$

### 3.3. The impact of displacement

As shown in Fig. 1,c, the snap-fit mechanism includes opposing hook and overhanging units which allow the structure to remain in a second (pressed) stable state. It requires a compression force and is stable only for certain unit cells such as V3.1 and V3.2 [47].

In the following section, an eigenfrequency study was performed for unit cells V3.1 and V3.2 considering a displacement of the snap-fit arms from 0.96 mm to 1.56 mm to study the change in frequency due to the transition to the second state.

Focusing on the audible range and displacement of 1.56 mm,  $\delta f$  varied up to 255 Hz (for V3.1) and 310 Hz (for V3.2), with exception at  $f_{0,V3.1} = 16\,192$  Hz with  $\delta f = -2369$  Hz, and  $f_{0,V3.1} = 19\,657$  Hz with  $\delta f = -1186$  Hz, as well as at  $f_{0,V3.2} = 16\,528$  Hz with  $\delta f = -2317$  Hz and  $f_{0,V3.2} = 19\,813$  Hz with  $\delta f = -1094$  Hz (Fig. 5). The impact of a displacement based deformation in the structure was more pronounced at higher frequencies. For example, a maximum shift to lower frequencies of  $-3542$  Hz and  $-2476$  Hz was predicted for the modes with initial eigenvalue of  $f_{0,V3.1} = 29\,133$  Hz and  $f_{0,V3.2} = 29\,267$  Hz.

In the next step, the change of  $\delta f$  by variation of the displacement was plotted for the six most affected modes and fitted with the function  $ax + b$  (Fig. 6). The calculated values for  $a$  and  $b$  are listed in Table 3. The linear relation facilitates a determination of the displacement of the sample based on the change in frequency and vice versa. Depending on whether a mode is dominated by the movement of the spring or arm element, it was influenced by the displacement to a different extent. Modes with pronounced deflection of the spring (I, II and III in Fig. 6) were more affected than those with more pronounced arm deflection (IV, V and VI). At 0.96 mm, regarding modes IV, V and VI  $\delta f$  varied between  $-309$  Hz and  $416$  Hz for V3.1, and  $-317$  Hz and  $401$  Hz for V3.2. While considering modes I, II and III, the obtained change in frequency was up to  $-2196$  Hz (V3.1) and  $1547$  Hz (V3.2). Further, at 1.56 mm,  $\delta f$  was in the range between  $-81$  Hz and  $100$  Hz (V3.1) and  $-88$  Hz and  $78$  Hz (V3.2) since the deformation in the arm element also decreased (see IV, V and VI) after passing the elevation. In contrast, the increase in displacement led to higher deformation of the spring and therewith to higher frequency shifts for frequencies dominated by the spring. For example,  $\delta f(x)$  showed the highest decrease for mode II (dominated by a deformation of the spring) as indicated by a negative slope of  $-2245$  Hz/mm for V3.1 and  $-1548$  Hz/mm for V3.2 (Fig. 6). Thus, also in the case of a displacement, only certain modes were significantly affected, so that these could be used as indicators, which a later acoustic resonance analysis can focus on.

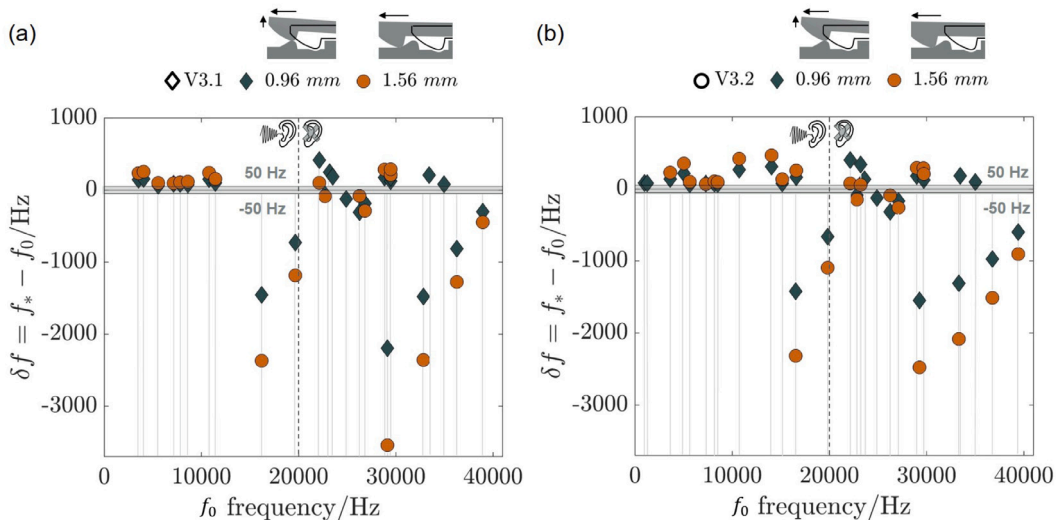


**Fig. 5.** Change in eigenfrequency as a result of a displacement from the initial state (black lines) for two unit cells: (a) V3.1 ( $b_{\text{spring}} = 1.5$  mm and  $b_{\text{snap}} = 4.5$  mm) and (b) V3.2 ( $b_{\text{spring}} = 3$  mm and  $b_{\text{snap}} = 4.5$  mm). At a displacement of 0.96 mm, a maximum deflection of the snap-fit arm is reached and at 1.56 mm, a maximum compression of the spring, corresponding to the second stable state, is obtained. Depicted are the cases in which  $\delta f > 50$  Hz. The complete data set is shown in Fig. A.10. The black arrows next to the pictograms refer to the direction of displacement.

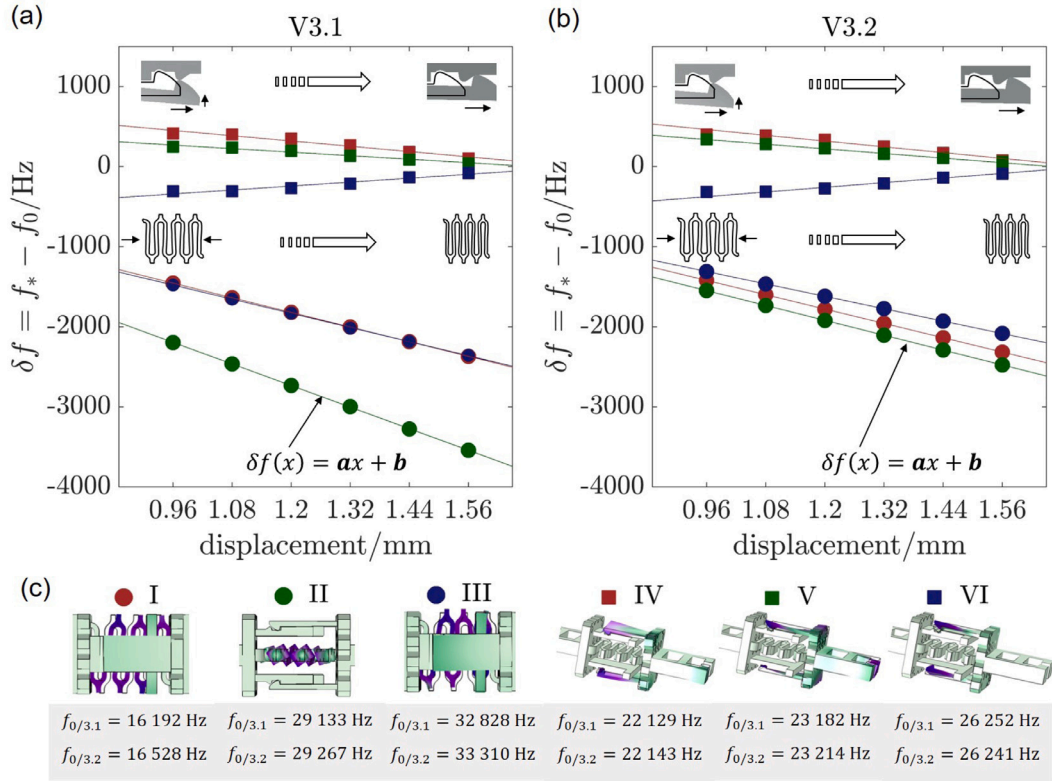


**Fig. 6.** Expected shift in natural frequency over the considered displacement range of 0.96 mm to 1.56 mm for selected vibration modes and two different unit cell types: (a) V3.1 and (b) V3.2. (c) The modes with the highest  $\delta f$  caused by this type of geometry change were selected. The regression functions were generated in Matlab and the coefficients determined can be found in Table 3 for the case of unit cell V3.1 ( $b_{\text{spring}} = 1.5$  mm and  $b_{\text{snap}} = 4.5$  mm, left) and V3.2 ( $b_{\text{spring}} = 3$  mm and  $b_{\text{snap}} = 4.5$  mm, right). The black arrows refer to the direction of displacement. (For interpretation of the references to colour in this figure legend, the reader is referred to the web version of this article.)

**Table 3**

Coefficients  $a$  and  $b$  related to the fit function  $\delta f = ax + b$  plotted in Fig. 6 and calculated by Matlab. The intersection point on the y-axis was set to zero.

V3.1			V3.2		
$f_0$ /Hz	$a$ /(Hz/mm)	$b$	$f_0$ /Hz	$a$ /(Hz/mm)	$b$
16 192	-1524	8	16 528	-1492	12
29 133	-2245	-39	29 267	-1548	-62
32 828	-1468	-70	33 310	-1289	-72
22 129	-550	980	22 143	-560	977
23 182	-367	621	23 214	-475	794
26 252	410	-735	26 241	414	-745

### 3.4. Variation in elastic modulus

An investigation of additively manufactured Ti6Al4V microbeams by Yin et al. [49] has shown a dependency of the mechanical properties on the specimen size and applied process parameters. The tested microbeams with process parameters adapted from that study were manufactured on the same machine and with the same process parameters as the unit cells examined in this work. In accordance with the related findings, the Young's modulus  $E$  was varied from 80 GPa to 140 GPa.

In the following section, the effect of Young's modulus variation on selected eigenfrequencies for a unit cell without defects was studied based on numerical simulations. The predicted change in eigenfrequency, caused by variation in  $E$ , is plotted in Fig. 7 for V1.2 and V3.1 as representatives for all sample types. Regardless of the unit cell type, a decrease in elastic modulus (80–100 GPa) led to a shift in all eigenvalues to lower frequencies, i.e. negative  $\delta f$  and in the case of an increase (120–140 GPa), vice versa. In Fig. 7 the change in  $\delta f$  is shown for cell V1.2 and V3.1 including all generated eigenvalues up to 40 kHz. For all natural modes, a deviation in  $E$  by 10 GPa, i.e. 9%, resulted in a frequency shift of 4 to 5%.

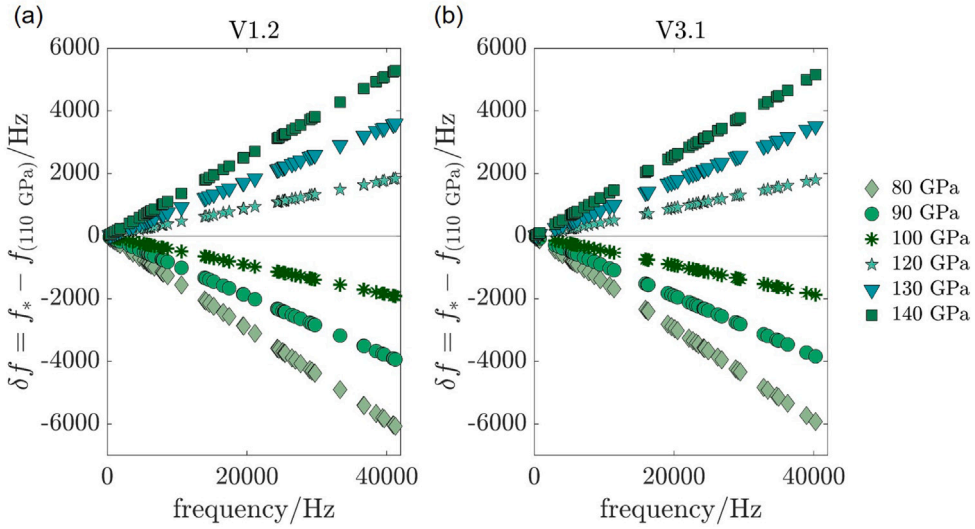


Fig. 7. Expected change in eigenfrequency,  $\delta f$ , considering a variation of the bulk elastic modulus (80 GPa to 140 GPa) for two unit cell types: (a) V1.2 ( $b_{\text{spring}} = 3 \text{ mm}$  and  $b_{\text{snap}} = 1.5 \text{ mm}$ ) and (b) V3.1 ( $b_{\text{spring}} = 1.5 \text{ mm}$  and  $b_{\text{snap}} = 3 \text{ mm}$ ). According to the materials data sheets for Ti6Al4V, the average nominal Young's modulus is 110 GPa and the natural frequencies computed for  $E = 110 \text{ GPa}$  are taken as a reference.

### 3.5. Multimodal frequency shift maps

In the previous paragraphs, the effect of design-related deviations (Fig. 2), manufacturing-related geometry deviation (Fig. 3), function-related geometry variation (Fig. 5) and Young's modulus variation (Fig. 7) were studied separately. However, they can occur simultaneously and superimpose for real parts. In order to be able to predict changes in the frequency of certain modes due to a combination of different deviations in the geometry or material properties, two exemplary frequency shift maps were generated for two unit cell geometries. Representative maps for the case of a variation in Young's modulus together with a distortion or displacement (compression) are shown in Fig. 8. For a selected eigenfrequency, there are instances where effects are negligible like the effect of distortion angle for V1.2 cell compared to the effect of Young's modulus (Fig. 8,a). In this case, the Young's modulus can be determined from the eigenfrequency independently from the distortion of the sample. In other cases (Fig. 8,b), ambiguities arise and the value of  $E$  has to be known in order to determine a change in the geometry due to displacement.

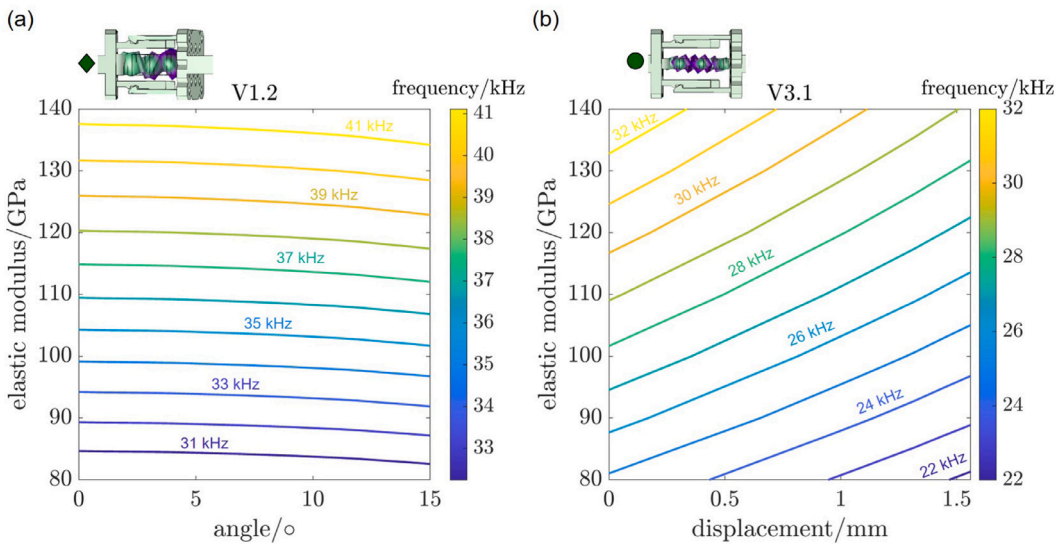


Fig. 8. Colour maps illustrating the expected frequency value of the natural mode depicted above by a given Young's modulus and (a) distortion angle (V1.2) or (b) displacement (V3.1).

Following this method, frequency shift maps can be created based on the synthetic data generated to determine the expected frequency change for a particular natural mode and guide experimental design as well as physical understanding of the acoustics of complex material systems. They enable to better interpret variability between measurements and identify frequency regions that are less affected by certain variations.

#### 4. Discussion

The present work focused on a systematical numerical evaluation of influence factors of additively manufactured structures on acoustic eigenfrequencies. Through the isolated analysis of deviations in geometry or material parameters, a prediction of their effect on the structure's vibration behaviour can be made and mode dependent effects can be identified.

A linear relation between the change in spring width, snap-fit width as well as Young's modulus as function of frequency was observed for selected modes in the simulations (Figs. 2 and 7). This effect can be derived from the simplified mathematical formula for eigenfrequencies of a single beam [50–52]:

$$f \propto \sqrt{\frac{EI}{\rho}} \quad (1)$$

where  $f$  designates eigenfrequencies,  $E$  the Young's modulus,  $I$  the second moment of inertia and  $\rho$  the density. This equation is based on a single Euler–Bernoulli beam, but can also be used as an approximation to explain trends in the vibration behaviour of the structure. In a very simplified way, metamaterials are constructed from beams with different cross-sections and in different orientations connected to each other. Therefore, the eigenfrequencies of beams with dimensions comparable to the dimensions of struts are good approximates for ART on metamaterials. For instance, according to the relation above, the increase in cross-section (defining the second moment of inertia) due to the higher width  $d$  (i.e. rod thickness) as well as an increase in the Young's modulus  $E$  both lead to higher frequency values.

In the present study, only global changes in Young's modulus were considered. Defects or structural deviations can entail local changes in stiffness, which affect only particular modes. Based on finite element simulations, in future studies, synthetic data could be generated for a wide range of local property changes such as density or Young's modulus variations.

According to Fig. 3, a deflection angle between 1° and 15° induced a measurable frequency shift (greater than 50 Hz) above 20 kHz and a displacement in the structure up to 1.56 mm (Fig. 5) already above 15 kHz. Thus, classifications with the target to detect these deviations should be carried out in the identified frequency ranges. However, this can also be advantageous as the effects will be negligible in the audible range and the method should be more precise towards other variations like the Young's modulus (Fig. 7) or geometrical features. In the range up to 10 kHz, results will be minimally affected by deflection and displacement.

Based on numerical simulations, mode dependent effects of design-, manufacturing- and function-specific factors were analysed. Resulting from this analysis, maps can be generated to visualize the interplay between different factors such as exemplary shown in Fig. 8. Mode dependent effect of irregularities has also been observed for wheel carrier [53] and connecting rods exhibiting drill holes with different diameter and position [45], but for the first time systematically studied for parameters specific to additively manufactured structures and a mechanical metamaterial unit cell. Although several factors were taken into account, there are also many more factors that can be studied including surface roughness, differences in manufacturing tolerance or presence of internal defects such as cracks or pores. In real structures, several defects can occur simultaneously and compensate or amplify their effects. For instance, an increase in Young's modulus can result in a peak shift to higher frequencies while a reduction in cross-section can cause a shift in the opposite direction. The presence of an open crack in a part can lead to a decrease in peak amplitude or the appearance of new peaks (indication for a higher harmonic oscillation) [54]. Further, a combination of various deviations may reflect in overlapping of two (or more) different spectral lines [53]. In the future, numerical design of experiments should be used to cover the vast parameter space and include as many variable parameters as possible.

Synthetic data can provide guidance for interpretation of experiments, but there are several aspects to consider. Not all predicted eigenfrequencies are experimentally detected and intensities of the eigenfrequencies vary. Boundary conditions, as well as the direction of the excitation, have a high impact on the vibration behaviour of rigid bodies. The present eigenfrequency study considered a free vibration state and variations due to experimental excitation or sample fixtures are thus not taken into account. FEM-based synthetic data generation can be automated so that it can form the basis for analysis of much more complex features of acoustic resonance spectra of additively manufactured samples in the future, for example, including variations of boundary conditions.

Tailoring the included parameter variations to specific experimental tasks is essential for transferring the knowledge to practical applications. For this purpose, experimental validation is an important next step to evaluate the benefit and restrictions of synthetic data sets. A purely experimental validation of the simulation results is very challenging, as it requires a statistically significant number of reference samples and, specifically, samples with defined defect variations. Large, controlled experimental data sets of parameter variations are still challenging and sometimes impossible to achieve as single parameters cannot be isolated. A future approach to manage validation of synthetic data could be the use of machine learning, trained with synthetic data, to predict the influencing factors of a given manufactured sample based on the acoustic spectrum. Machine learning has been already applied in the acoustic resonance analysis of metallic lattice structures [15,55], ripeness of watermelons [12] and glass bottles [10]. In this case, it would support the experimental validation and possibly enable the faster adaptation of ART to new base materials, processes or metamaterial designs.

## 5. Conclusions

The application of acoustic resonance analysis to test complex structures such as metamaterial unit cells and structures remains a challenge. Based on a systematic variation of parameters, numerical simulations revealed mode dependent influence of isolated as well as overlapping parameter changes on the vibration modes of complex geometries.

Deviations of the geometry affect eigenfrequencies depending on the specific vibration modes. Local geometrical variations mainly affect the modes where these areas of the samples experience high deflections. The eigenfrequency mode dominated by the spring around 3 kHz shows a linear increase in eigenfrequency with increasing spring width and no effect from snap-fit width. In contrast, the eigenfrequency mode dominated by the snap-fit between 3.5 and 5.5 kHz shows an increase in eigenfrequency with increasing snap-fit width while the spring width has a minor effect. Distortion of the cell up to 15° and a displacement up to 1.56 mm leads to a predicted frequency change below 50 Hz in the frequency range below 10 kHz, so that, experimentally, such defects are difficult to detect. To enable detection of these variations, measurements should focus on a higher frequency range. In contrast, measurements independent of these parameters can be expected at frequencies beyond 10 kHz. A deviation of the elastic modulus affects all eigenfrequencies due to the underlying mechanical eigenfrequency formation in structures. A shift of the whole spectrum of 4 to 5 % from the nominal state was observed when the elastic modulus changes by 10 GPa.

In practice, isolated effects rarely occur in additively manufactured structures. A combination of varied parameters is usually present and relevant for future applications. Therefore, multiparameter studies were performed and colour plots derived. The visualization provides an intuitive impression of the mode specific importance or unimportance of certain parameters and an estimation of the expected frequency shifts.

Synthetic data, as presented in this work, provide a basis to understand the complex interplay of overlapping factors on the acoustic spectra of additively manufactured materials. However, there are many challenges to experimentally validate the results and translate the findings for quality inspection. More extensive designs of numerical experiments, including factors such as boundary conditions and local parameter variations, are required. Complementing the multidimensional parameter variations, the use of data analysis methods like machine learning could help to identify unknown superimposed parameters in experimental data to improve interpretation of the results and speed up the adaptation of ART to a new part in industry. Acoustic resonance testing remains very attractive for industrial applications because of the cost-efficiency and scalability to production scale, but more research is necessary in the future to mitigate some of the current limitations.

### CRedit authorship contribution statement

**Silviya M. Boyadzhieva:** Writing – review & editing, Writing – original draft, Visualization, Validation, Methodology, Formal analysis, Conceptualization. **Florian Gutmann:** Resources. **Sarah C.L. Fischer:** Writing – review & editing, Validation, Supervision, Resources, Methodology, Conceptualization.

### Declaration of competing interest

The authors declare that they have no known competing financial interests or personal relationships that could have appeared to influence the work reported in this paper.

### Data availability

Data will be made available on request.

### Acknowledgements

All authors would like to acknowledge discussions with colleagues at Fraunhofer IZFP, Fraunhofer EMI and within the Cluster of Excellence Programmable Materials, especially Konstantin Kappe and Ute Rabe. This work was supported by a Fraunhofer Internal Program, Germany under the Grand No. Attract 025 - 601314 awarded to S.C.L Fischer. This work was also partially funded by Fraunhofer Cluster of Excellence “Programmable Materials”, Germany.

### Appendix. Further numerical results

The effect of distortion (Fig. 3) and displacement (Fig. 6) were described in the main manuscript. The display was limited to all eigenfrequencies with a shift of 50 Hz or higher caused by the change in geometry. In this appendix, we provide the reader with an overview of all eigenfrequencies computed in the simulation for a distortion of 15° for V1.2 and V1.3 (Fig. A.9) as well as a displacement of up to 1.5 mm for V3.1 and V3.2 (Fig. A.10).

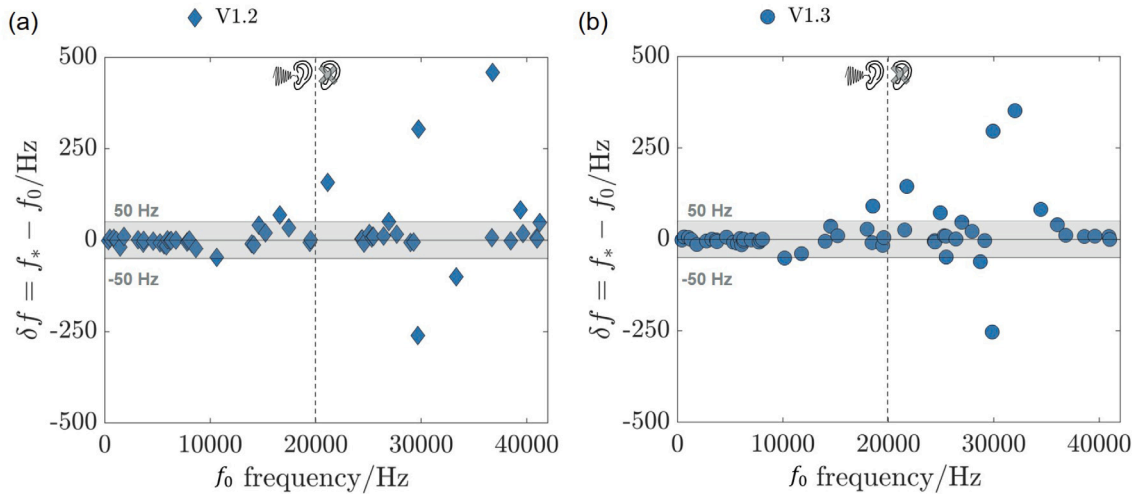


Fig. A.9. Predicted shift in natural frequency due to structure distortion of  $15^\circ$  in the case of two unit cells: (a) V1.2 ( $b_{\text{spring}} = 3$  mm and  $b_{\text{snap}} = 1.5$  mm) and (b) V1.3 ( $b_{\text{spring}} = 4.5$  mm and  $b_{\text{snap}} = 1.5$  mm).

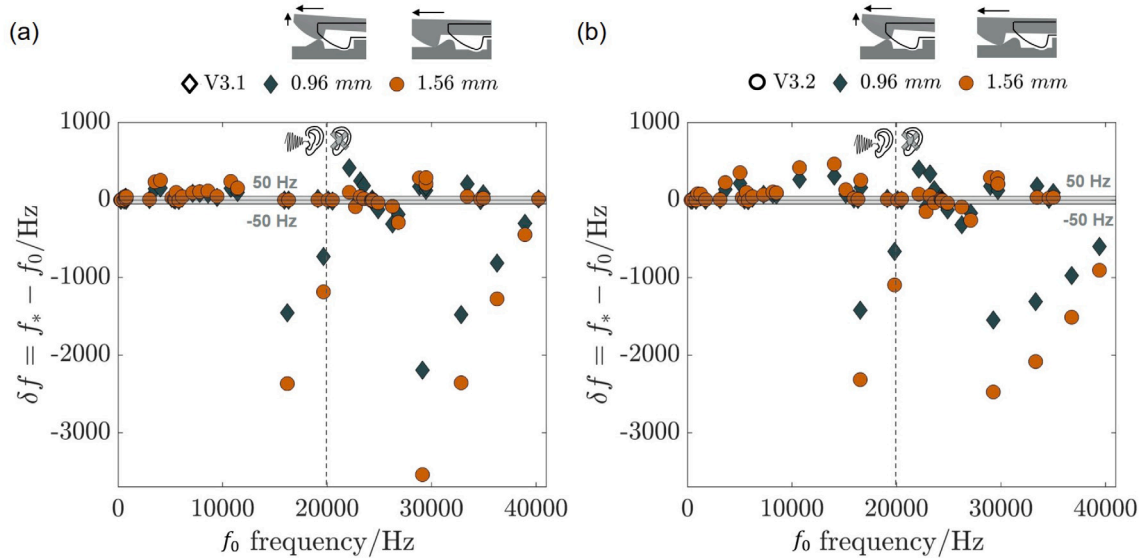


Fig. A.10. Change in eigenfrequency as a result of a displacement from the initial state for two unit cell types: (a) V3.1 and (b) V3.2. At displacement of 0.96 mm a maximum deflection of the snap-fit arm is reached and at 1.56 mm maximum compression of the spring in the second stable state.

## References

- [1] R.D. Adams, P. Cawley, C.J. Pye, B.J. Stone, A vibration technique for non-destructively assessing the integrity of structures, *J. Mech. Eng. Sci.* 20 (2) (1978) 93–100, [http://dx.doi.org/10.1243/JMES\\_JOUR\\_1978\\_020\\_016\\_02](http://dx.doi.org/10.1243/JMES_JOUR_1978_020_016_02).
- [2] G. Hearn, R. Testa, Modal analysis for damage detection in structures, *J. Struct. Eng.* 117 (7) (1991) 3042–3063, [http://dx.doi.org/10.1061/\(ASCE\)0733-9445\(1991\)117:10\(3042\)](http://dx.doi.org/10.1061/(ASCE)0733-9445(1991)117:10(3042)).
- [3] R.W. Bono, G.R. Stultz, Resonant inspection applied to 100% testing of nodularity of cast ductile iron, *SAE Int. J. Passeng. Cars - Mech. Syst.* 1 (1) (2009) 1247–1250, <http://dx.doi.org/10.4271/2008-01-2577>.
- [4] Y.C. Ju, I. Kraljevski, H. Neunübel, C. Tschöpe, M. Wolff, Acoustic resonance testing of small data on sintered cogwheels, *Sensors* 22 (15) (2022) 5814, <http://dx.doi.org/10.3390/s22155814>.
- [5] I. Hertlin, K. Heldmann, Acoustic resonance analysis for crack detection and structure testing in series production: Process and examples, *Giesserei* 87 (3) (2000) 51–54.
- [6] C. Lai, X. Sun, C. Dasch, G. Harmon, M. Jones, Quantify resonance inspection with finite element-based modal analyses, *J. Vib. Acoust.* 133 (3) (2011) 031004, <http://dx.doi.org/10.1115/1.4002955>.
- [7] S. Biswas, C. Monroe, Identifying cast iron microstructure variation using acoustic resonance techniques, *Int. J. Met.* 13 (1) (2019) 26–46, <http://dx.doi.org/10.1007/s40962-018-0241-4>.

- [8] I. Kraljevski, F. Duckhorn, Y.C. Ju, C. Tschoepe, C. Richter, M. Wolff, Acoustic resonance recognition of coins, in: 2020 IEEE International Instrumentation and Measurement Technology Conference (I2MTC), Dubrovnik, Croatia, 2020, pp. 1–6, <http://dx.doi.org/10.1109/I2MTC43012.2020.9129256>.
- [9] S. Levikari, T.J. Karkkainen, C. Andersson, J. Tamminen, P. Silventoinen, Acoustic phenomena in damaged ceramic capacitors, *IEEE Trans. Ind. Electron.* 65 (1) (2018) 570–577, <http://dx.doi.org/10.1109/TIE.2017.2714123>.
- [10] I. Kraljevski, F. Duckhorn, Y.C. Ju, C. Tschoepe, M. Wolff, Acoustic resonance testing of glass IV bottles., in: *Artificial Intelligence Applications and Innovations*, Vol. 584, Springer International Publishing, Cham, Switzerland, 2020, pp. 195–206, [http://dx.doi.org/10.1007/978-3-030-49186-4\\_17](http://dx.doi.org/10.1007/978-3-030-49186-4_17).
- [11] Z. Fathizadeh, M. Aboonajmi, S.R.H. Beygi, Nondestructive firmness prediction of apple fruit using acoustic vibration response, *Sci. Hortic.* 262 (2020) 109073, <http://dx.doi.org/10.1016/j.scienta.2019.109073>.
- [12] D. Albert-Weiss, A. Osman, Interactive deep learning for shelf life prediction of muskmelons based on an active learning approach, *Sensors* 22 (2) (2022) 414, <http://dx.doi.org/10.3390/s22020414>.
- [13] Y. Ibrahim, Z. Li, C.M. Davies, C. Maharaj, J.P. Dear, P.A. Hooper, Acoustic resonance testing of additive manufactured lattice structures, *Addit. Manuf.* 24 (2018) 566–576, <http://dx.doi.org/10.1016/j.addma.2018.10.034>.
- [14] S.M. Boyadzhieva, L.S. Kollmannsperger, F. Gutmann, T. Straub, S.C.L. Fischer, Acoustic nondestructive characterization of metal pantographs for material and defect identification, in: S.L. Kramer, E. Retzlaff, P. Thakre, J. Hoefnagels, M. Rossi, A. Lattanzi, F. Hemez, M. Mirshekari, A. Downey (Eds.), *Additive and Advanced Manufacturing, Inverse Problem Methodologies and Machine Learning and Data Science*, Vol. 4, Springer Nature Switzerland, Cham, Switzerland, 2024, pp. 47–53, [http://dx.doi.org/10.1007/978-3-031-50474-7\\_7](http://dx.doi.org/10.1007/978-3-031-50474-7_7).
- [15] A.-F. Obaton, Y. Wang, B. Butsch, Q. Huang, A non-destructive resonant acoustic testing and defect classification of additively manufactured lattice structures, *Weld World* 65 (2021) 361–371, <http://dx.doi.org/10.1007/s40194-020-01034-7>.
- [16] L. Dong, W.P. King, M. Raleigh, H.N. Wadley, A microfabrication approach for making metallic mechanical metamaterials, *Mater. Des.* 160 (2018) 147–168, <http://dx.doi.org/10.1016/j.matdes.2018.09.008>.
- [17] M. Dallago, B. Winiarski, F. Zanini, S. Carmignato, M. Benedetti, On the effect of geometrical imperfections and defects on the fatigue strength of cellular lattice structures additively manufactured via selective laser melting, *Int. J. Fatigue* 124 (2019) 348–360, <http://dx.doi.org/10.1016/j.ijfatigue.2019.03.019>.
- [18] F. Zanini, M. Sorgato, E. Savio, S. Carmignato, Uncertainty of CT dimensional measurements performed on metal additively manufactured lattice structures, in: *10th Conference on Industrial Computed Tomography*, Vol. 25, e-Journal of Nondestructive Testing, Wels, Austria, 2020, <http://dx.doi.org/10.58286/25084>.
- [19] S.C.L. Fischer, L. Hillen, C. Eberl, Mechanical metamaterials on the way from laboratory scale to industrial applications: Challenges for characterization and scalability, *Materials* 13 (16) (2020) 3605, <http://dx.doi.org/10.3390/ma13163605>.
- [20] J.U. Surjadi, L. Gao, H. Du, X. Li, X. Xiong, N.X. Fang, Y. Lu, Mechanical metamaterials and their engineering applications, *Adv. Eng. Mater.* 21 (3) (2019) 1800864, <http://dx.doi.org/10.1002/adem.201800864>.
- [21] L. Fok, M. Ambati, X. Zhang, Acoustic metamaterials, *MRS Bull.* 33 (10) (2008) 931–934, <http://dx.doi.org/10.1557/mrs2008.202>.
- [22] M. Specht, M. Berwind, C. Eberl, Adaptive wettability of a programmable metasurface, *Adv. Eng. Mater.* 23 (2) (2021) 2001037, <http://dx.doi.org/10.1002/adem.202001037>.
- [23] K. Bertoldi, V. Vitelli, J. Christensen, M. van Hecke, Flexible mechanical metamaterials, *Nat. Rev. Mater.* 2 (11) (2017) 17066, <http://dx.doi.org/10.1038/natrevmats.2017.66>.
- [24] Y. Zhang, L. Wang, W. Gao, T. Gu, Z. Li, X. Li, R. Li, G. Ye, W. Jiang, Y. Zhu, H. Liu, Bioinspired from butterfly wings: programmable actuation of isolated rods architectures for magnetic-assisted microswitches, *Smart Mater. Struct.* 28 (7) (2019) 075014, <http://dx.doi.org/10.1088/1361-665X/ab1163>.
- [25] P.U. Kelkar, H.S. Kim, K.-H. Cho, J.Y. Kwak, C.-Y. Kang, H.-C. Song, Cellular auxetic structures for mechanical metamaterials: A review, *Sensors* 20 (11) (2020) 3132, <http://dx.doi.org/10.3390/s20113132>.
- [26] J.T.B. Overvelde, S. Shan, K. Bertoldi, Compaction through buckling in 2D periodic, soft and porous structures: Effect of pore shape, *Adv. Mater.* 24 (17) (2012) 2337–2342, <http://dx.doi.org/10.1002/adma.201104395>.
- [27] T. Frenzel, M. Kadic, M. Wegener, Three-dimensional mechanical metamaterials with a twist, *Science* 358 (6366) (2017) 1072–1074, <http://dx.doi.org/10.1126/science.aao4640>.
- [28] T.A. Schaedler, A.J. Jacobsen, A. Torrents, A.E. Sorensen, J. Lian, J.R. Greer, L. Valdevit, W.B. Carter, Ultralight metallic microlattices, *Science* 334 (6058) (2011) 962–965, <http://dx.doi.org/10.1126/science.1211649>.
- [29] T. Gustmann, F. Gutmann, F. Wenz, P. Koch, R. Stelzer, W.-G. Drossel, H. Korn, Properties of a superelastic NiTi shape memory alloy using laser powder bed fusion and adaptive scanning strategies, *Prog. Addit. Manuf.* 5 (1) (2020) 11–18, <http://dx.doi.org/10.1007/s40964-020-00118-6>.
- [30] X. Kuang, J. Wu, K. Chen, Z. Zhao, Z. Ding, F. Hu, D. Fang, H.J. Qi, Grayscale digital light processing 3D printing for highly functionally graded materials, *Sci. Adv.* 5 (5) (2019) eaav5790, <http://dx.doi.org/10.1126/sciadv.aav5790>.
- [31] C. Xu, B. Quinn, L.L. Lebel, D. Theriault, G. L'Espérance, Multi-material direct ink writing (DIW) for complex 3D metallic structures with removable supports, *ACS Appl. Mater. Interfaces* 11 (8) (2019) 8499–8506, <http://dx.doi.org/10.1021/acsami.8b19986>.
- [32] S.M. Montgomery, X. Kuang, C.D. Armstrong, H.J. Qi, Recent advances in additive manufacturing of active mechanical metamaterials, *Curr. Opin. Solid State Mater. Sci.* 24 (5) (2020) 100869, <http://dx.doi.org/10.1016/j.cossms.2020.100869>.
- [33] Y. Shen, W. Cantwell, R. Mines, Y. Li, Low-velocity impact performance of lattice structure core based sandwich panels, *J. Compos. Mater.* 48 (25) (2014) 3153–3167, <http://dx.doi.org/10.1177/0021998313507616>.
- [34] C. Zitelli, P. Folgarait, A. Di Schino, Laser powder bed fusion of stainless steel grades: A review, *Metals* 9 (7) (2019) 731, <http://dx.doi.org/10.3390/met9070731>.
- [35] V. Sufiiarov, V. Sokolova, E. Borisov, A. Orlov, A. Popovich, Investigation of accuracy, microstructure and properties of additive manufactured lattice structures, *Mater. Today Proc.* 30 (2020) 572–577, <http://dx.doi.org/10.1016/j.matpr.2020.01.137>.
- [36] M. Colopi, A.G. Demir, L. Caprio, B. Previtali, Limits and solutions in processing pure cu via selective laser melting using a high-power single-mode fiber laser, *Int. J. Adv. Manuf. Technol.* 104 (5–8) (2019) 2473–2486, <http://dx.doi.org/10.1007/s00170-019-04015-3>.
- [37] Q. Jiang, P. Zhang, Z. Yu, H. Shi, D. Wu, H. Yan, X. Ye, Q. Lu, Y. Tian, A review on additive manufacturing of pure copper, *Coatings* 11 (6) (2021) 740, <http://dx.doi.org/10.3390/coatings11060740>.
- [38] L. Dong, Mechanical response of Ti–6Al–4V hierarchical architected metamaterials, *Acta Mater.* 175 (2019) 90–106, <http://dx.doi.org/10.1016/j.actamat.2019.06.004>.
- [39] A. Falkowska, A. Seweryn, M. Skrodzki, Strength properties of a porous titanium alloy Ti6Al4V with diamond structure obtained by laser powder bed fusion (LPBF), *Materials* 13 (22) (2020) 5138, <http://dx.doi.org/10.3390/ma13225138>.
- [40] T. Macoachie, M. Leary, B. Lozanovski, X. Zhang, M. Qian, O. Faruque, M. Brandt, SLM lattice structures: Properties, performance, applications and challenges, *Mater. Des.* 183 (2019) 108137, <http://dx.doi.org/10.1016/j.matdes.2019.108137>.
- [41] S. Ahmadi, R. Hedayati, R. Ashok Kumar Jain, Y. Li, S. Leeftang, A. Zadpoor, Effects of laser processing parameters on the mechanical properties, topology, and microstructure of additively manufactured porous metallic biomaterials: A vector-based approach, *Mater. Des.* 134 (2017) 234–243, <http://dx.doi.org/10.1016/j.matdes.2017.08.046>.
- [42] H. Gong, K. Rafi, H. Gu, G. Janaki Ram, T. Starr, B. Stucker, Influence of defects on mechanical properties of Ti–6Al–4V components produced by selective laser melting and electron beam melting, *Mater. Des.* 86 (2015) 545–554, <http://dx.doi.org/10.1016/j.matdes.2015.07.147>.

- [43] M. Heinrich, U. Rabe, B. Valeske, Simulation-based generation of representative and valid training data for acoustic resonance testing, *Appl. Sci. - Basel* 10 (17) (2020) 6059, <http://dx.doi.org/10.3390/app10176059>.
- [44] M. Xu, Z. Qiu, Free vibration analysis and optimization of composite lattice truss core sandwich beams with interval parameters, *Compos. Struct.* 106 (2013) 85–95, <http://dx.doi.org/10.1016/j.compstruct.2013.05.048>.
- [45] M. Heinrich, B. Valeske, U. Rabe, Efficient detection of defective parts with acoustic resonance testing using synthetic training data, *Appl. Sci. - Basel* 12 (15) (2022) 7648, <http://dx.doi.org/10.3390/app12157648>.
- [46] P. Lechner, E. Reberger, M. Gruber, S. Kammerloher, C. Hartmann, W. Volk, Localization of cavities in cast components via impulse excitation and a finite element analysis, *Prod. Eng. Res. Dev.* 16 (6) (2022) 869–877, <http://dx.doi.org/10.1007/s11740-022-01134-x>.
- [47] K. Kappe, J.P. Wahl, F. Gutmann, S.M. Boyadzhieva, K. Hoschke, S.C.L. Fischer, Design and manufacturing of a metal-based mechanical metamaterial with tunable damping properties, *Materials* 15 (16) (2022) 5644, <http://dx.doi.org/10.3390/ma15165644>.
- [48] T.R. Jebieshia, J.M. Kim, J.W. Kang, S.W. Son, H.D. Kim, Microstructural and very high cycle fatigue (VHCF) behavior of Ti6Al4V-A comparative study, *Materials* 13 (8) (2020) 1948, <http://dx.doi.org/10.3390/ma13081948>.
- [49] K. Yin, B. Cao, J. Todt, F. Gutmann, H.F. Tunçay, A. Roth, F. Fischer, N. Grübel, A. Pfaff, G.C. Ganzenmüller, J. Keckes, S. Hiermaier, C. Eberl, Manufacturing size effect on the structural and mechanical properties of additively manufactured Ti-6Al-4V microbeams, *J. Mater. Sci. Technol.* 149 (2023) 18–30, <http://dx.doi.org/10.1016/j.jmst.2022.12.006>.
- [50] L. Schmidt, R. Steinbuch, Improved interpretation of the acoustic response spectrum to identify types of component deviations, *Res. Nondestruct. Eval.* 14 (2) (2002) 95–110, <http://dx.doi.org/10.1007/s00164-001-0024-8>.
- [51] P. Hagedorn, A. DasGupta, Vibrations of beams, in: *Vibrations and Waves in Continuous Mechanical Systems*, John Wiley & Sons, Ltd, Hoboken, New Jersey, USA, 2007, pp. 113–178, <http://dx.doi.org/10.1002/9780470518434.ch3>.
- [52] A.G. Piersol, T.L. Paez, C.M. Harris, *Harris' Shock and Vibration Handbook*, 6. ed., McGraw-Hill handbooks, McGraw-Hill, New York, NY, 2010.
- [53] R. Steinbuch, Scatter or defect? Some remarks on the interpretation of acoustic spectral shift, *Res. Nondestruct. Eval.* 15 (4) (2005) 173–189, <http://dx.doi.org/10.1080/09349840490915645>.
- [54] A. Migot, V. Giurgiutiu, Numerical and experimental investigation of delamination severity estimation using local vibration techniques, *J. Intell. Mater. Syst. Struct.* 34 (9) (2023) 1057–1072, <http://dx.doi.org/10.1177/1045389X221128585>.
- [55] A.-F. Obaton, N. Fallahi, A. Tanich, L.-F. Lafon, G. Weaver, Statistical analysis and automation through machine learning of resonant ultrasound spectroscopy data from tests performed on complex additively manufactured parts, *J. Nondestruct. Eval.* 43 (2024) 24, <http://dx.doi.org/10.1007/s10921-023-01035-8>.